Single-Receiver Multioutput Inductive Power Transfer System With Independent Regulation and Unity Power Factor

Xiaoqiang Wang, Jianping Xu, *Member, IEEE*, Song Lu, Sheng Ren, Minrui Leng, *Student Member, IEEE*, and Hongbo Ma, *Member, IEEE*

***Abstract*—Inductive power transfer (IPT) systems with multiple output voltages are potential to supply a variety of loads simultaneously. This article proposes an IPT system with multiple semiactive rectifier cells (SARCs) connected in series at the receiver (Rx) side. These SARCs are independent of each other and their output voltages can be regulated individually with single receiver coil, which reduces the cost and volume. The proposed IPT configuration has the advantages of high flexibility, simple control, and no cross regulation. Considering that the SARC may cause additional reactance and lead to detuning of the Rx side, variable inductor is introduced to ensure the full tuning condition. Thus, the proposed IPT system can maintain zero phase angle operation with unity power factor in the whole load range, minimizing the reactive power losses. In addition, both primary inverter and the SARCs can achieve zero voltage switching. To verify the feasibility and validity of the proposed IPT system, an experimental prototype with two outputs of 640 W/150 V and 400 W/120 V is built.**

***Index Terms*—Individually regulated multioutput, inductive power transfer (IPT), semiactive rectifier cells (SARCs), unity power factor, zero voltage switching (ZVS).**

I. Introduction

INDUCTIVE power transfer (IPT) technology for wirelessly charged devices have attracted enormous attention in recent years due to its extensive advantages, e.g., environmental friendliness, isolation, convenience, reliability, etc. The IPT technology has been applied in numerous applications such as biomedical implants [1], [2], consumer electronics [3] and, electric vehicles [4]–[7]. Conventionally, a simple two-coil IPT system, which consists of a transmitter (Tx) and a receiver (Rx), is used to power the load. However, such two-coil IPT system can only provide one output voltage [8].

Manuscript received December 15, 2020; revised March 17, 2021 and May 31, 2021; accepted July 17, 2021. Date of publication July 27, 2021; date of current version September 16, 2021. This work was supported by the National Natural Science Foundation of China under Grants 51777176 and 61733015. Recommended for publication by Associate Editor X. Ruan. *(Corresponding author: Hongbo Ma.)*

The authors are with the School of Electrical Engineering, Southwest Jiaotong University, Chengdu 610031, China, and also with the Key Laboratory of Magnetic Suspension Technology and Maglev Vehicle, Ministry of Education, Chengdu 611756, China (e-mail: xqwang0621@163.com; jpxu-swjtu@163.com; lusong@my.swjtu.edu.cn; ren3040@qq.com; mrleng_pece@163.com; mahongbo81@gmail.com).

Color versions of one or more figures in this article are available at https://doi.org/10.1109/TPEL.2021.3100055.

Digital Object Identifier 10.1109/TPEL.2021.3100055

In some applications, e.g., the dc motor drives and neural stimulators for biomedical devices, multiple supply voltages are required [9], [10]. For example, the neurostimulation requires dual higher voltages by the stimuli generator for small amount of current injected in the tissue, while a low voltage would be used by the read-out circuitries [10]. In addition, the hybrid energy storage system also requires multiple voltage levels for different charging modes (i.e., rapid charging, smart charging, and normal charging) [11].

Till now, various approaches have been reported to obtain multioutput IPT systems. A simple way to obtain multioutput is to connect multiple separate dc–dc converters in parallel to the common port of the Rx [11], [12]. Intuitively, this system architecture seems to be the simplest approach because it has the advantages of flexible control and no cross regulation. Nevertheless, multiple dc–dc converters need large number of components, which will cause large volume and cost. Besides, more power conversion stages inevitably degrade the transfer efficiency.

In order to reduce the power conversion stages, multi-Tx multi-Rx IPT systems are proposed in [13]–[16] to implement multiple outputs. In [13], multiple Txs and the corresponding compensation networks share the same primary inverter. All Txs are not always activated together at the same time because each of them is turned ON or OFF by using a contactor. As a consequence, stray field and losses are significantly reduced. In [14] and [15], single-inductor multiple-output based dc–ac inverter for driving multiple independent high-frequency ac outputs is proposed. Unfortunately, the issues of numerous components and large volume still exist in these works [13]–[16].

To further simplify circuit structure and reduce component count, single-Tx multi-Rx IPT system is proposed in [17]–[21]. The multiple Rx can be supplied simultaneously by the same Tx. However, the mutual couplings between multiple Rxs and the Tx are highly dependent on their relative positions. Hence, the control of multiple outputs is quite difficult. In order to eliminate/suppress the cross-effect between receiver coils, the flux cancellation method and circuit-based decoupling methods have been proposed in [22] and [23]. However, these decoupling methods only suitable to dual-output IPT system, which can hardly accommodate an arbitrary number of general outputs. In addition, a flexible load-independent multioutput IPT system with one transmitter coil and one receiver coil is developed in [24] and [25]. By connecting multiple T-type compensation

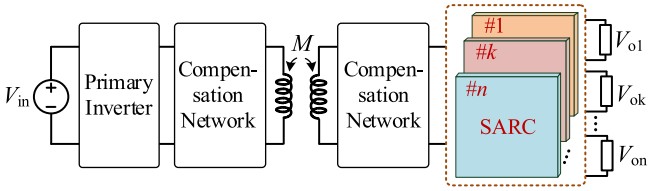

Fig. 1. Proposed structure of multioutput IPT system based on SARCs.

topologies in parallel to the common ac terminal of the receiver coil, multiple load-independent constant dc output voltages, or currents can be achieved. The major drawbacks of this multicompensation-topology method is that the output voltage or current in each channel cannot be regulated individually, which restricts its further development in practical applications.

According to the literatures, the multioutput IPT system is mainly obtained by extending the magnetic coupled coil or the compensation network while fewer works concentrate on the extension of the rectifier. Actually, the component count of the magnetic coupled coil and the compensation network can be reduced as much as possible if only multiple active rectifiers are applied. Although the active rectifier has been extensively studied [26]–[29], so far little attention has been paid to the utilization of multiple active rectifiers cells (SARCs) to achieve multiple output voltages.

As indicated in [30], the equivalent input impedance of the SARC should be capacitive so that the SARC can achieve zero voltage switching (ZVS). In this case, the Rx side of the IPT system would detune, which cause large reactive power losses. Therefore, it is of great importance to maintain the resonant condition of the IPT system. Impedance adjustment based on variable capacitor or variable inductor is one of the commonly used dynamic tuning method [31]–[35]. Generally, variable capacitor can be classified into two categories: capacitor matrix and switch-controlled capacitor. Although variable capacitor can be integrated with compensation capacitors, there are still some drawbacks. For example, capacitor matrix only produces discrete capacitance, the resolution of the tuning is limited. In addition, switched-controlled capacitor needs synchronization signals, which increases the circuit complexity. The switches may also suffer from high voltage stress, which poses a great challenge on component selection [32]. For variable inductor [37]–[39], the inductance is regulated by changing the dc bias current of control winding. Thus, continuous tuning inductance can be produced without any synchronization signals. Besides, the switches and the driver circuits are not required, which can reduce the volume and cost. Considering the dc bias current is small, the power loss of the control winding is ignorable. As a result, variable inductor is applied to tune the Rx dynamically.

In this article, a multioutput IPT system based on multiple SARCs is proposed, as illustrated in Fig. 1. The SARCs are independent of each other and connected in series at the Rx side, with their output voltages being regulated individually. The proposed SARCs-based IPT system has advantages of high generality for extension, simple control, high flexibility, and no cross-regulation issue. In addition, only single receiver coil is utilized. Thus, the favorable advantage of reduced cost and volume is retained.

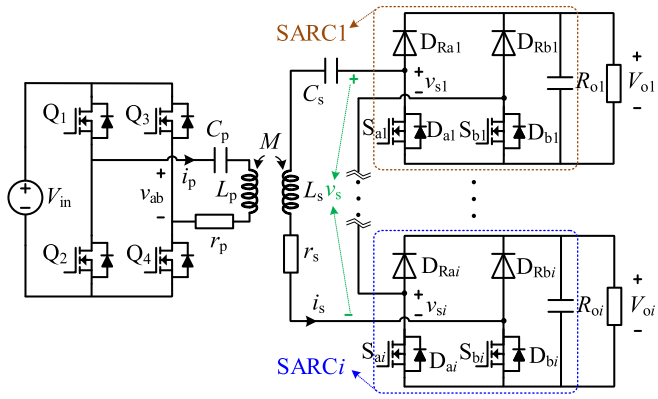

Fig. 2. Main circuit of the proposed multioutput IPT system.

On the other hand, variable inductor is employed to tune the Rx dynamically. Therefore, in the proposed IPT system, zero phase angle (ZPA), namely unity power factor between the inverter output current and voltage, is ensured in the whole load range, which can minimize the reactive power losses. Moreover, both the inverter and the SARCs can achieve ZVS.

This article is organized as follows. Section II introduces the proposed multioutput IPT system. As an example, a dual-output one is analyzed in detail to comprehensively show the performance characteristics. Subsequently, the implementation of the proposed control method and design considerations are demonstrated in Sections III and IV, respectively. Experimental results are given in Section V. Finally, Section VI concludes this article.

II. Proposed Multioutput IPT System

A. System Modeling

As shown in Fig. 1, multiple SARCs are connected in series at the Rx side and controlled independently. For the analysis of the circuit characteristics, a multioutput IPT system is depicted in Fig. 2. The series–series compensation topology is energized by MOSFETs Q_1–Q_4 and their corresponding antiparallel diodes. The magnetic coupled coils have Tx self-inductance L_p, Rx self-inductance L_s, and mutual inductance M. The coupling coefficient is defined as $k = M/(L_pL_s)^{1/2}$. C_p and C_s are the compensation capacitances of Tx coil and Rx coil, respectively. The equivalent series resistances (ESRs) of the coils r_p and r_s are taken into consideration for the purpose of analyzing system efficiency. The SARCi ($i = 1, 2, \ldots n$) consists of two diodes D_{Rai} and D_{Rbi} in the upper legs, and two MOSFETs S_{ai} and S_{bi} in the lower legs. D_{ai} and D_{bi} are the antiparallel body diodes of S_{ai} and S_{bi}, respectively. In the proposed IPT system, the primary switches always operate with a fixed frequency ω and a fixed duty cycle of 50%. For simplicity, the fundamental harmonic approximation method is used.

As shown in Fig. 2, v_{ab} is the equivalent output ac voltage of the primary inverter. v_{si} is the equivalent input ac voltage of the SARCi. In the following analysis, V_{ab} and $\boldsymbol{V}_{ab}$ are adopted to represent the root-mean-square (rms) and the phasor of v_{ab}, respectively, and other variables are denoted in a similar way.

The equivalent ac circuit of the proposed IPT system is shown in Fig. 3. The SARCi together with the load resistance R_{oi} can be

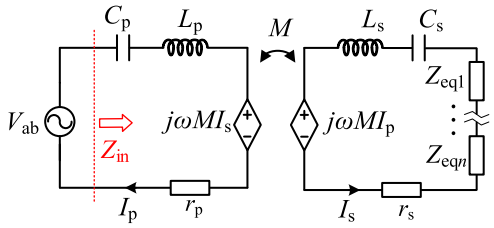

Fig. 3. Equivalent ac circuit of the proposed IPT system.

represented by an equivalent ac impedance $Z_{eqi} = R_{eqi} + jX_{eqi}$, which will be analyzed in Section II-B. The input impedance of the proposed IPT system is defined as Z_{in}.

By using Kirchhoff voltage law in Fig. 3, the IPT system can be described by the following equations:

$$\begin{cases} V_{ab} = Z_p I_p + j\omega M I_s \\ 0 = j\omega M I_p + Z_s I_s \end{cases} \tag{1}$$

where the impedance of the Tx and the Rx are given by

$$\begin{cases} Z_p = j\omega L_p + 1/j\omega C_p + r_p = jX_p + r_p \\ Z_s = j\omega L_s + 1/j\omega C_s + jX_{eq1} + \cdots \\ \quad +jX_{eqn} + r_s = jX_s + r_s \end{cases} \tag{2}$$

with X_p and X_s are the equivalent reactance in the Tx side and the Rx side, respectively. n is integer. If X_p (X_s) is equal to zero, the Tx (Rx) side is fully compensated.

Substituting (2) into (1), the currents of the Tx coil and the Rx coil can be calculated as

$$I_p = V_{ab}\sqrt{A_{p\_re}^2 + A_{p\_im}^2}\Big/ B_p \tag{3a}$$

$$I_s = V_{ab}\sqrt{A_{s\_re}^2 + A_{s\_im}^2}\Big/ B_p \tag{3b}$$

where A_{p_re}, A_{p_im}, A_{s_re}, A_{s_im}, and B_p are given as follows:

$$\begin{aligned} A_{p\_re} &= \omega^2 M^2 \left(r_s + \sum_{i=1}^{n} R_{eqi}\right) \\ &\quad + r_p \left[\left(r_s + \sum_{i=1}^{n} R_{eqi}\right)^2 + X_s^2\right] \\ A_{p\_im} &= -X_p \left(r_s + \sum_{i=1}^{n} R_{eqi}\right)^2 + \omega^2 M^2 X_s - X_p X_s^2 \\ A_{s\_re} &= \omega M \left[r_p X_s + X_p \left(r_s + \sum_{i=1}^{n} R_{eqi}\right)\right] \\ A_{s\_im} &= \omega M \left[X_p X_s - \omega^2 M^2 - r_p \left(r_s + \sum_{i=1}^{n} R_{eqi}\right)\right] \end{aligned} \tag{4a}$$

$$\begin{aligned} B_p &= \left(X_p^2 + r_p^2\right)\left[\left(r_s + \sum_{i=1}^{n} R_{eqi}\right)^2 + X_s^2\right] \\ &\quad + 2\omega^2 M^2 \left[-X_p X_s + r_p \left(r_s + \sum_{i=1}^{n} R_{eqi}\right) + \omega^2 M^2/2\right]. \end{aligned} \tag{4b}$$

The system efficiency is

$$\begin{aligned} \eta &= \frac{P_{out}}{P_{in}} = \frac{\omega^2 M^2}{A_{p\_re}} \sum_{i=1}^{n} R_{eqi} \\ &= \frac{\omega^2 M^2 \sum_{i=1}^{n} R_{eqi}}{\omega^2 M^2 \left(r_s + \sum_{i=1}^{n} R_{eqi}\right) + r_p \left[\left(r_s + \sum_{i=1}^{n} R_{eqi}\right)^2 + X_s^2\right]}. \end{aligned} \tag{5}$$

It can be seen from (5) that the system efficiency η has no relation with Tx-side reactance X_p, but it is a function against Rx- side reactance X_s and equivalent ac loads R_{eqi}. As X_s is a part of the denominator of (5), the larger reactance of the Rx side will result in a lower system efficiency for the given loads R_{eqi}. As a consequence, in order to improve the system efficiency, X_s should be eliminated to zero, namely, the Rx side should be fully tuned.

On the other hand, the input impedance of the proposed IPT system can be derived as

$$Z_{in} = B_p \left(A_{p\_re} - jA_{p\_im}\right)\Big/ \sqrt{A_{p\_re}^2 + A_{p\_im}^2}. \tag{6}$$

According to [13], ZPA operation of the IPT system is preferred to minimize the volt-ampere rating of the power supply. Thus, the imaginary part of (6) should be zero so that the input impedance Z_{in} is purely resistive. On the premise of $X_s = 0$, it only needs to make $X_p = 0$ to achieve ZPA operation. Thus, both the Tx side and the Rx side should be fully tuned for a high system performance. As a consequence, based on (2), the following equations are required to be satisfied:

$$\omega L_p - 1/\omega C_p = 0, \omega L_s - 1/\omega C_s + \sum_{i=1}^{n} X_{eqi} = 0. \tag{7}$$

From (3) and (7), the Rx coil current is simplified as

$$I_s = \frac{\omega M V_{ab}}{\omega^2 M^2 + r_p \left(r_s + \sum_{i=1}^{n} R_{eqi}\right)} \approx \frac{V_{ab}}{\omega M}. \tag{8}$$

From (8), it can be found that I_s is load-independent under the assumption that $r_p << \omega M$ and $r_s << \omega M$. This assumption is reasonable because the coils' ESR is quite small for high efficiency [41]. It should be noted that with a relatively large coil current, nonignorable voltage drop occurs on the ESRs and thereby the fully tuned Tx side is no longer valid. Therefore, load-independent Rx coil current cannot be obtained, which in turn results in cross-regulation issues. However, in most IPT systems, the influences on voltage regulation are quite small, which is acceptable in practical applications.

Considering that increasing or decreasing of the number of SARCs in Rx side has no influence on the operation of the proposed multioutput IPT system. As an example, only two SARCs connected in series at the Rx side are taken into consideration to demonstrate the performance of the proposed multioutput IPT system.

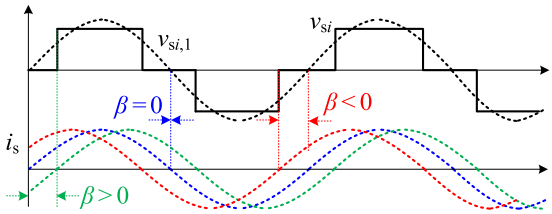

Fig. 4. Waveforms of SARC*i* under different operation modes.

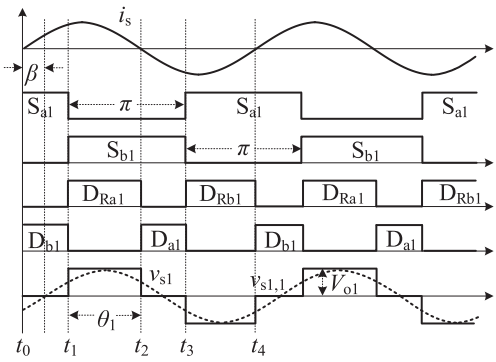

Fig. 5. Key waveforms of SARC1 under capacitive operation mode.

B. Operation of the SARC

According to the phase difference β between the input current i_s and the input voltage $v_{si,1}$ of SARC*i*, SARC has three possible operation modes, $\beta<0$, $\beta=0$ and $\beta>0$, as depicted in Fig. 4, where $v_{si,1}$ represents the fundamental component of v_{si}. $\beta>0$ means that i_s lags behind $v_{si,1}$ and SARC*i* operates in inductive mode. $\beta=0$ means that i_s and $v_{si,1}$ is in phase and SARC*i* operates in resistive mode. $\beta<0$ means that i_s leads $v_{si,1}$ and SARC*i* operates in capacitive mode. It has been proven in [30] that SARC*i* should operate in capacitive mode to achieve ZVS. As a consequence, an extra capacitive reactance X_{eqi} will be introduced at the Rx side.

As an example, Fig. 5 shows the key waveforms of SARC1 operating in capacitive mode. As can be seen, there are four different stages in a switching cycle. Due to the symmetry of the current waveform, only half of the switching period is described in detail.

Stage I [t_0–t_1]: During this interval, switch S_{a1} is turned ON, diode D_{Ra1} and switch S_{b1} are in OFF-state. The cycle starts with positive current i_s and the current flows through S_{a1} and D_{b1}. The voltage v_{s1} equals to zero, as shown in Fig. 5.

Stage II [t_1–t_2]: At t_1, switch S_{a1} is turned OFF, diode D_{Ra1} and switch S_{b1} are both in ON-state. The current i_s flows through S_{b1} and D_{Ra1}. During this interval, the voltage v_{s1} equals to V_{o1}, as shown in Fig. 5.

Obviously, MOSFETs S_1 and S_2 are turned ON during the on-time of their antiparallel diodes to have ZVS. Both S_1 and S_2 are turned ON for half a cycle, and they are complements of each other. The conduction angle of SARC1 is defined as $\theta_1\in[0, \pi]$, which determines the output voltage to fulfill the practical requirement. For a positive half-cycle of current i_s, S_2 is turned ON with a time delay of $\pi-\theta$ to the zero-crossing point where i_s commutates from negative to positive. In a similar way, with the same time delay to the next zero-crossing point where i_s commutates from positive to negative, S_1 is turned ON for half a cycle.

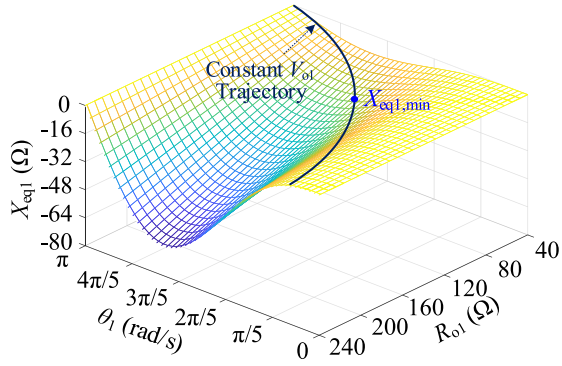

Fig. 6. Three-dimensional surface of X_{eq1} versus different R_{o1} and θ_1.

According to Fig. 5, the phase difference β can be derived as

$$\beta = (\theta_1 - \pi)/2. \tag{9}$$

The magnitude of $v_{s1,1}$ is determined by the control angle θ_1 and the output voltage V_{o1}. The terminal voltage $\boldsymbol{V}_{s1}$ of SARC1 is given as

$$\boldsymbol{V}_{s1} = \frac{2\sqrt{2}}{\pi} V_{o1} \sin\frac{\theta_1}{2} e^{-j\beta} \tag{10}$$

where $\boldsymbol{V}_{s1}$ is the phasor of v_{s1}.

The dc output current filtered by the output capacitor can be derived by

$$I_{o1} = \frac{2\sqrt{2}}{\pi} I_s \sin\frac{\theta_1}{2} \cos\beta. \tag{11}$$

By calculating the ratio of $\boldsymbol{V}_{s1}$ and $\boldsymbol{I}_s$ and substituting (9) into (10) and (11), the SARC1 together with the resistive load R_{o1} can be represented by an equivalent impedance $Z_{eq1} = R_{eq1} + jX_{eq1}$, where

$$R_{eq1} = \frac{8}{\pi^2} R_{o1} \sin^4\frac{\theta_1}{2} \tag{12}$$

$$X_{eq1} = -\frac{8}{\pi^2} R_{o1} \sin^3\frac{\theta_1}{2} \cos\frac{\theta_1}{2}. \tag{13}$$

In addition, combining (8), (9), and (11), the output voltage of SARC1 can be calculated as

$$V_{o1} = \frac{2\sqrt{2}}{\pi} \frac{V_{ab}}{\omega M} R_{o1} \sin^2\frac{\theta_1}{2}. \tag{14}$$

From (14), it can be known that the output voltage V_{o1} is inversely proportional to mutual inductance M, but in proportion to equivalent ac input voltage V_{ab} and load resistance R_{o1}. When V_{ab}, M, or R_{o1} changes, the control angle θ_1 should be adjusted accordingly to maintain the constant output voltage.

According to (13), the three-dimensional surface of X_{eq1} versus different R_{o1} and θ_1 is shown in Fig. 6. It can be seen that when R_{o1} is fixed, with the increase of θ_1, X_{eq1} decreases and then increases. On the other hand, X_{eq1} decreases accordingly with the increase of R_{o1}. In the following analysis, the subscripts "min" and "max", respectively, represent the minimum and maximum of the corresponding variables. Considering that the

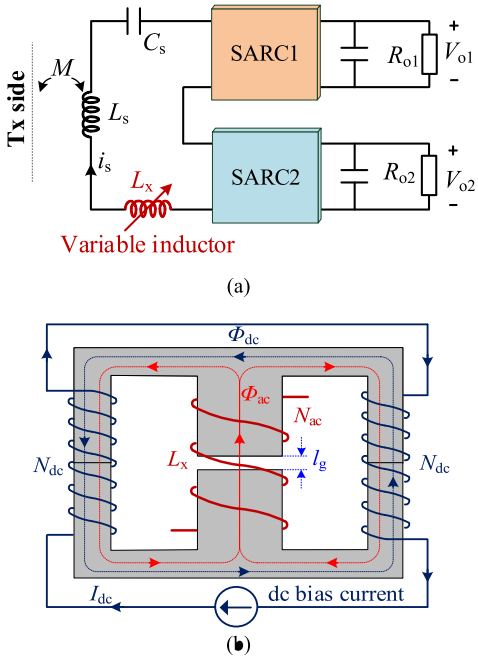

Fig. 7. Circuit diagram. (a) Proposed IPT system with variable inductor. (b) Variable inductor using double E core and a dc bias current.

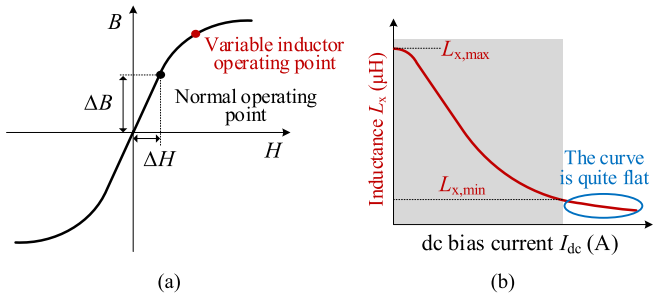

Fig. 8. Key curves of variable inductor. (a) *B-H* curve. (b) Inductance value versus dc bias current of a variable inductor.

TABLE I
SPECIFICATIONS OF THE PROPOSED IPT SYSTEM

Parameter	Symbol	Value
Input DC voltage	V_{in}	160V
Rated output voltage of channel 1	V_{o1}	150V
Rated output power of channel 1	P_{o1}	640W
Rated output voltage of channel 2	V_{o2}	120V
Rated output power of channel 2	P_{o2}	400W
Switching angular frequency	ω	2π×85kHz
Air gap between Tx coil and Rx coil	A_g	150mm

range of θ_1 is $[0, \pi]$, it can be derived from (13) that $X_{eq1}(\theta_1 = 0) = X_{eq1}(\theta_1 = \pi) = 0$, i.e., $X_{eq1,max} = 0$. Thus, X_{eq1} is always negative regardless of the variation of R_{o1} and θ_1. From (14), to maintain constant output voltage V_{o1}, the larger R_{o1} is, the smaller θ_1 is, as the trajectory depicted in Fig. 6. Namely, for a given load, there must have a minimum value of X_{eq1}, which is denoted as $X_{eq1,\,min}$.

C. Operation of the Variable Inductor

It is preferred to maintain the resonant condition in both the Tx side and the Rx side. As an extra capacitive reactance X_{eqi} caused by SARC*i* is introduced in the Rx side, variable inductor [36]–[39] is, thus, applied in this article to dynamically adjust the impedance of the Rx, as shown in Fig. 7(a). The variable inductor with double E core is demonstrates in Fig. 7(b). The main winding, i.e., inductor L_x, with the number turns of N_{ac}, is placed on the air-gapped middle leg of the core. The control winding is divided into two identical portions with the number of turns N_{dc}, and it is mounted on the outer, nongaped legs of the core. The two portions of the control winding are connected in series but with opposite polarity.

This structure has the advantage that the ac coupling between the main winding and the control winding is cancelled. Thus, the resonant voltage across the main winding will not induce ac voltage in the control windings.

The main idea of the variable inductor is that, with the increase of the dc bias current I_{dc}, the operating points of the outer legs on the *B-H* curve move from the linear region to the partial saturation region [39], as shown in Fig. 8(a). Hence, the incremental permeability of the outer legs decreases, which results in a decreased inductance L_x, as shown in Fig. 8(b). It can be seen from Fig. 8(b) that when the dc bias current is zero, the inductance L_x reaches the maximum inductance $L_{x,max}$. With a larger dc bias current, the L_x-I_{dc} curve becomes quite flat, which indicates a reduction of the loop gain. Besides, higher conduction losses of the control winding are inevitable. Therefore, it is preferable to make the variable inductor operate within the shadow region.

III. Design Consideration and Control Strategy

A. Design of the Magnetic Coupler

The magnetic coupler with large air gaps is essential to an IPT system. Various coil structures are reported [3], [22] and the popular circular coil structure are selected in this article. The specifications of the proposed IPT system are shown in Table I. Practically, the proposed multioutput IPT system is applicable to various applications, such as medical equipment, household appliance and electric vehicles, etc. As an example, the voltage and power level listed in Table I is much suitable for automatic guided vehicles battery charging [40].

The maximum output current I_{om} is defined as

$$I_{om} = \max\{P_{oi}/V_{oi}\}, i = 1, 2 \tag{15}$$

where $\max\{P_{oi}/V_{oi}\}$ is the maximum of P_{oi}/V_{oi}.

According to (8) and (11), it can be found that I_{oi} is inversely proportional to the mutual inductance M. Although the output voltages are the control targets, the maximum allowable output current should be estimated for the design of the magnetic coupler. Considering that the Rx coil current becomes larger under misaligned conditions as per the series–series topology, the IPT system is controllable as long as the maximum output current can be obtained with the largest M. As a consequence, the design of the magnetic coupler is carried out in well-aligned case. According to (8), (9), and (11), when $\theta_i = \pi$, the mutual

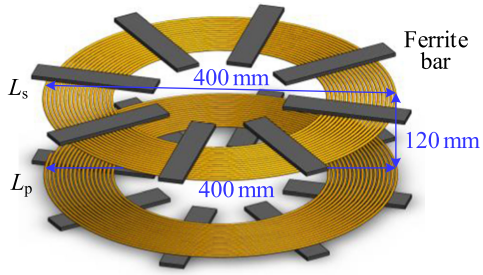

Fig. 9. Dimensions and airgap of the magnetic coupler.

inductance M in well-aligned case can be calculated as

$$M_{\max} = \frac{2\sqrt{2}V_{\mathrm{ab}}}{1.05\pi\omega I_{\mathrm{om}}} \tag{16}$$

where the factor 1.05 represents that some margin is taken into consideration when design the mutual inductance. That is because (8) is deduced on the premise of fully tuned Tx side and thereby the practical Rx coil current is bound to be slightly smaller than the calculated value. Although a larger factor, such as 1.1, 1.15, etc., can be also chosen to make the IPT system controllable, the maximum control angle of SARC*i* will deviate from π significantly. In other words, the Rx coil current could not be made full use, which increases the conduction losses.

To fulfill the requirement of (16), the finite-element analysis software Maxwell is employed. Generally, the dimensions and airgap of the magnetic coupler are given according to practical applications [41], [42]. The ferrite bars are adopted to enhance the coupling, as shown in Fig. 9.

As indicated in [43], there is an optimal load resistance $R_{\mathrm{eq,opt}}$ for the maximum system efficiency under the condition where $X_{\mathrm{p}} = X_{\mathrm{s}} = 0$, which can be expressed as

$$R_{\mathrm{eq,opt}} = \sqrt{r_{\mathrm{s}}\left(\omega^2 M^2 + r_{\mathrm{p}} r_{\mathrm{s}}\right)/r_{\mathrm{p}}} \approx \omega M\sqrt{r_{\mathrm{s}}/r_{\mathrm{p}}}. \tag{17}$$

As can be seen, (17) cannot be always hold since the mutual inductance M and load resistance vary with coil misalignments and the output power, respectively. In this article, the efficiency optimization is performed at full load and well-aligned case. In addition, it is assumed that $\theta_{\mathrm{i}} = \pi$ at full load. Then, combining (12) and (15)–(17), the relationship between coil's ESR, i.e., r_{p} and r_{s}, can be derived as

$$\frac{r_{\mathrm{s}}}{r_{\mathrm{p}}} = \frac{64(R_{\mathrm{o1}} + R_{\mathrm{o2}})^2}{\pi^4\omega^2 M_{\max}^2}. \tag{18}$$

Since the coil's ESR is dependent on the corresponding turn number, can be selected as a simple criterion of the optimization of the magnetic coupler. The design flow of the magnetic coupler is depicted in Fig. 10.

According to the design flow, the turn numbers of L_{p} and L_{s} are selected as 15 and 17, respectively. The measured self- and mutual inductances versus misalignments are shown in Fig. 11. As can be seen, the self-inductances L_{p} and L_{s} almost maintain constant regardless of the variation of misalignments. Namely, the misalignment has no influence on the tuning condition in both sides. In this article, it is assumed that the maximum horizontal misalignment of the magnetic coupler is 100 mm. Consequently, according to Fig. 11, the available range of the

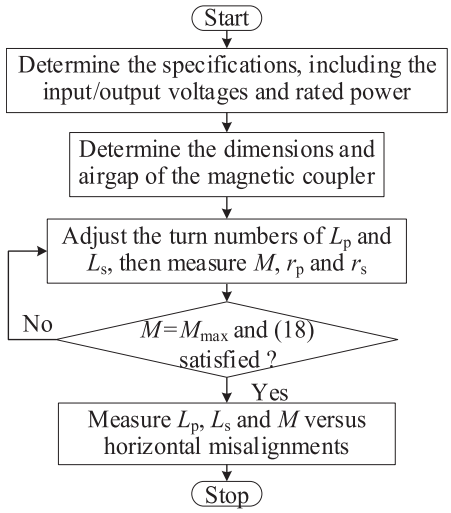

Fig. 10. Design flow of the magnetic coupler.

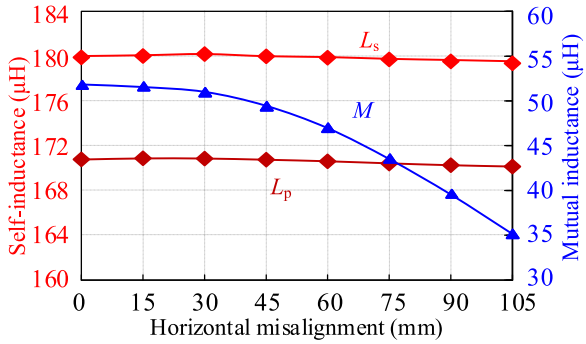

Fig. 11. Measured self- and mutual inductances versus the horizontal coil misalignments.

coupling coefficient $[k_{\min}, k_{\max}]$ can be given as

$$k_{\min} = M_{\min}\Big/\sqrt{L_p L_s} = 0.2, k_{max} = M_{\max}\Big/\sqrt{L_p L_s} = 0.3. \tag{19}$$

B. Design of the Variable Inductor

The variable inductor design procedure begins by selecting the desirable inductance range $[L_{\mathrm{x,min}}, L_{\mathrm{x,max}}]$. For simplification, the ratio of $L_{\mathrm{x,max}}$ and $L_{\mathrm{x,min}}$ is defined as

$$\lambda = L_{x,\max}/L_{x,\min} > 1. \tag{20}$$

According to (7) and Fig. 6(a), the following equation should be satisfied:

$$\omega L_{\mathrm{s}} - 1/\omega C_{\mathrm{s}} + X_{\mathrm{eqt}} + \omega L_{\mathrm{x}} = 0. \tag{21}$$

To determine the inductance range of L_{x}, the total reactance $X_{\mathrm{eqt}} = X_{\mathrm{eq1}} + X_{\mathrm{eq2}}$ should be determined first. Combining (8), (9), (11), and (13), the total reactance X_{eqt} can be calculated as

$$X_{\mathrm{eqt}} = \sum_{i=1,2} X_{\mathrm{eq}i} = -\sum_{i=1,2} \frac{\omega M V_{\mathrm{o}i}}{V_{\mathrm{in}}} \sin\frac{\theta_i}{2}\cos\frac{\theta_i}{2}. \tag{22}$$

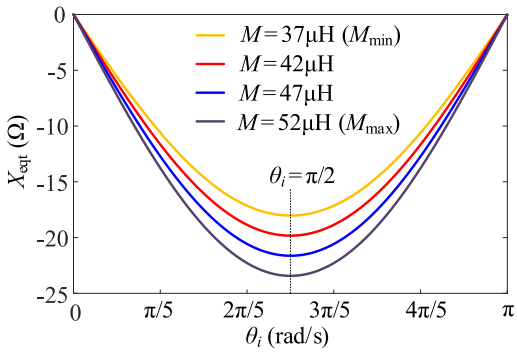

Fig. 12. Curve of X_{eqt} versus θ_i with different mutual inductance M.

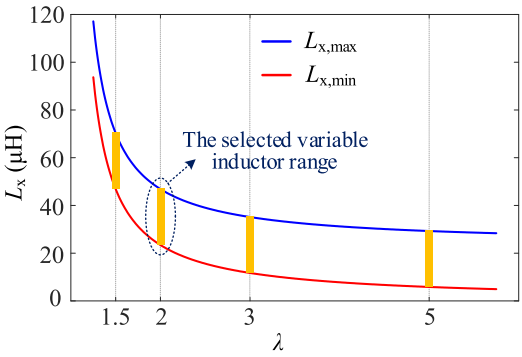

Fig. 13. Required variable inductance range with different λ.

It can be known from (22) that X_{eqt} has no relation to the load $R_{\mathrm{o}i}$. Combining (22) and the specifications listed in Table I, the curve of X_{eqt} versus θ_i is depicted in Fig. 12. It can be found that for a given M, X_{eqt} reaches its minimum when $\theta_i = \pi/2$. In Practical application, it is possible that $\theta_1 = \theta_2 = \pi/2$ because both SARC1 and SARC2 are regulated independently. Then, by substituting $\theta_i = \pi/2$ and $M = M_{\max}$ into to (22), X_{eqt} can be calculated as

$$X_{\mathrm{eqt,min}} = -\frac{\omega M_{\max}}{2V_{\mathrm{in}}}\left(V_{\mathrm{o1}} + V_{\mathrm{o2}}\right). \tag{23}$$

According to Fig. 12, it can be seen that X_{eqt} is always negative because $X_{\mathrm{eqt,max}} = 0$, and thereby a smaller X_{eqt} requires a larger L_{x} so that the Rx side can be fully tuned within the entire load range. In other words, (21) can be rewritten as

$$\begin{cases} \omega L_{\mathrm{s}} - 1/\omega C_{\mathrm{s}} + X_{\mathrm{eqt,max}} + \omega L_{\mathrm{x,min}} = 0 \\ \omega L_{\mathrm{s}} - 1/\omega C_{\mathrm{s}} + X_{\mathrm{eqt,min}} + \omega L_{\mathrm{x,max}} = 0. \end{cases} \tag{24}$$

Combining (20), (23), (24), Table I, and Fig. 12, the required variable inductance range with different λ is shown in Fig. 13. As can be seen, with a smaller λ, the inductance L_{x} becomes larger, which results in higher conduction loss. However, when λ becomes large, the inductance L_{x} is quite small, which means a high dc bias current is needed. As a compromise, λ is selected as 2, and the desired variable inductance range $[L_{\mathrm{x,min}}, L_{\mathrm{x,max}}]$ is [24 μH, 48 μH] when considering some margin.

In this article, an EE70 core with PC40 material is selected to implement the variable inductor. A flux limit of 0.1 T will be used in this design to reduce the impact of residual coupling. According to [36], the number of turns for the main winding and the control winding can be, respectively, estimated by

$$N_{\mathrm{ac}} = \frac{L_{\mathrm{x,max}} I_{\mathrm{s,max}}}{0.1 B_{\mathrm{sat}} A_e}, N_{\mathrm{dc}} = \frac{1}{2}\frac{B_{\mathrm{sat}} l_{\mathrm{ext}}}{\mu I_{\mathrm{dc,max}}} \tag{25}$$

where B_{sat} is the saturation flux density. l_{ext} is the length of the external path and A_{e} is the effective area of the core, which can be obtained from the datasheet.

Actually, (25) only represents a brief guidance of the turn number design for the variable inductor, which is a simplified and approximate method. The experimental parameters of the variable inductor are listed in Table II.

The measured inductance of the variable inductor, by using an LCR meter (Model 11025), is depicted in Fig. 14. Within the operating range of the variable inductor, the measured results can be fitted by a polynomial curve with the help of MATLAB. The corresponding fitting function can be represented as

$$\begin{aligned} L_{\mathrm{x}} &= \Psi\left(I_{\mathrm{dc}}\right) \\ &= \sum_{n=0,1,2\ldots}^{m} p_n I_{\mathrm{dc}}^n \, or \, I_{\mathrm{dc}} = \Psi^{-}\left(L_{\mathrm{x}}\right) = \sum_{n=0,1,2\ldots}^{m} q_n L_{\mathrm{x}}^n \end{aligned} \tag{26}$$

where Ψ^{-} is the inverse function of Ψ; p_n and q_n are the coefficients of Ψ and Ψ^{-}, respectively; n and m are integers.

It should be emphasized that the maximum dc bias current is approximately 2 A, and thereby the power loss of the control winding is less than 5 W, which is not included in the measurements of system efficiency.

TABLE II
PARAMETERS OF THE VARIABLE INDUCTOR

Parameter	Symbol	Value
Ferrite cores	–	PC40
Ferrite material	–	EE70
Effective area	A_{e}	573mm^2
Turn number of the main winding	N_{ac}	13
ESR of the main winding	r_{x}	23 mΩ
Turn number of the control winding	N_{dc}	70
ESR of the control winding	r_{cw}	1.08 Ω
Litz wire for the main winding	–	0.1mm×600
Litz wire for the control winding	–	0.1mm×40
Air gap of the middle leg	l_g	5mm

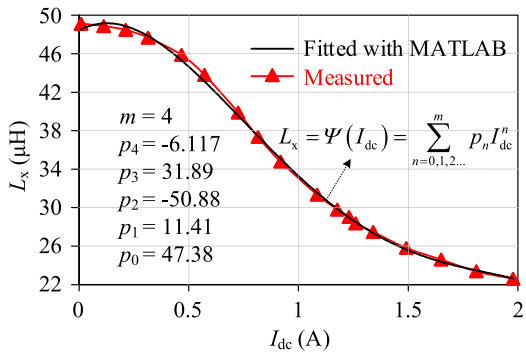

Fig. 14. Measured inductance of the variable inductor.

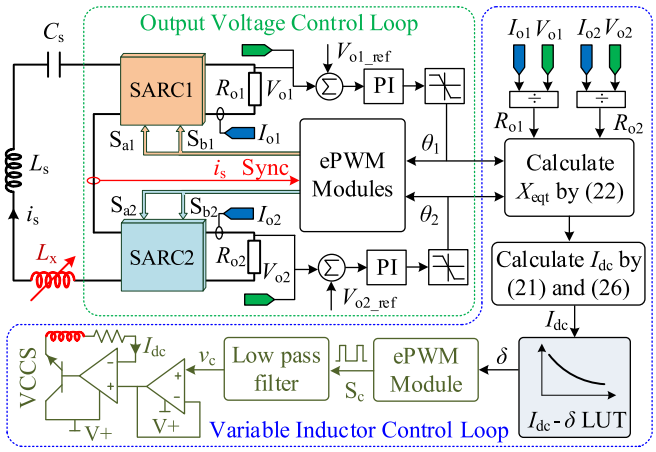

Fig. 15. Diagram of the proposed control strategy. Note: S_{ai} and S_{bi} are the driver signals of SARCi and sync is the abbreviation of synchronization.

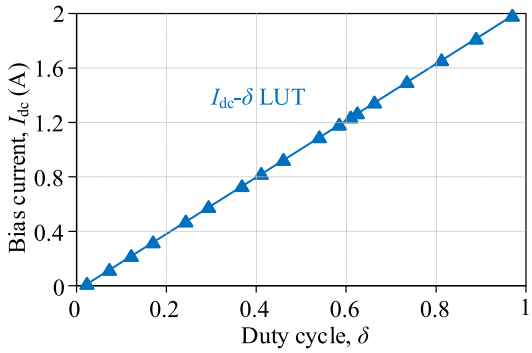

Fig. 16. I_{dc}-δ LUT based on the measurement results.

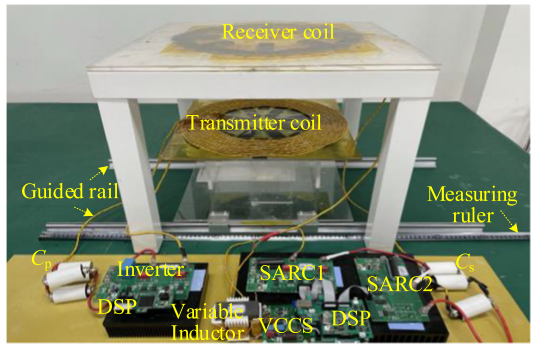

Fig. 17. Photograph of experiment prototype.

TABLE III
PARAMETERS OF THE PROPOSED IPT SYSTEM

Parameter	Symbol	Value
Self-inductance of Tx coil	L_p	169.6 μH
Tx-side compensation capacitor	C_p	20.6 nF
ESR of Tx coil	r_p	252 mΩ
Mutual Inductance (k=0.3)	M	52 μH
Self-inductance of Rx coil	L_s	179.6 μH
Rx-side compensation capacitor	C_s	17.6 nF
ESR of Rx coil	r_s	265 mΩ

C. Implementation of the Control Strategy

The diagram of the proposed control strategy is illustrated in Fig. 15. Since the proposed control strategy is based on fixed switching frequency and Rx-side real-time regulation, wireless feedback communication is not required. The output voltages V_{oi} and currents I_{oi} are measured by sensors. The load resistance R_{oi} can be calculated by the divider. Regarding to the output voltage control loop, two separate PI controllers are applied to correct the difference between V_{oi} and V_{oi_ref}, and forms the corresponding control signal θ_i for the SARCi. Meanwhile, the Rx coil current is detected to provide the synchronization signal for the SARCi.

Traditionally, for the purpose of tuning the Rx side, the resonant condition in Rx side should be detected by measuring the phase difference between the induced voltage and current with auxiliary measurement coils [30], [44], which inevitably makes the control circuits complicated. In this article, the control signal of variable inductor is generated according to the analytical relationship and the I_{dc}-δ look-up table (LUT), where δ is the duty cycle of square wave S_c, as shown in the variable inductor control loop.

In order to decrease the effect of output voltage control loop on the variable inductor control loop, the setting time of output control loop is relatively longer than that of variable inductor loop. Therefore, the control signals θ_i and the load resistance R_{oi} can be obtained from the DSP controller to calculate X_{eqt} by (22). Then, the required dc bias current I_{dc} is calculated by (21) and (26). Once the value of I_{dc} is determined, the corresponding dc bias current can be generated by a voltage controlled current source (VCCS). For this target, a square wave S_c with duty cycle δ is filtered through a low-pass filter to form the dc control voltage v_c of VCCS. As analyzed previously, there is a unique combination of I_{dc} and δ that corresponds to the fully tuned Rx side, and the I_{dc}-δ LUT is established on the basis of measurement results, as shown in Fig. 16.

Theoretically, the small-signal model of IPT systems can be established to analyze the closed loop behavior. For example, series–series IPT systems with near resonant operations can be properly modeled for small-signal behavior [45], [46]. However, different from the existing works [45] and [46], in which the authors have only focused on single-output IPT system, the small-signal model for multioutput IPT system is bound to be a more complicated work. This article pays more attention to propose the circuit structure of the multioutput IPT system with high flexibility and simple control. Undoubtedly, the small-signal model of multioutput IPT system is also an interesting and valuable work, which will be investigated in our future works.

IV. EXPERIMENTAL VERIFICATIONS

In order to verify the proposed multioutput IPT system, an experiment prototype with 640 W/150 V and 400 W/120 V outputs is fabricated, as shown in Fig. 17. When the magnetic coupled coils are in well-aligned case, the electrical parameters of the IPT system are given in Table III. The MOSFETs (C3M0030090K) are chosen for the full-bridge inverter and the SARCi. A digital power analyzer, PW6001 from HIOKI, is used to analyze the efficiency of the multioutput IPT system.

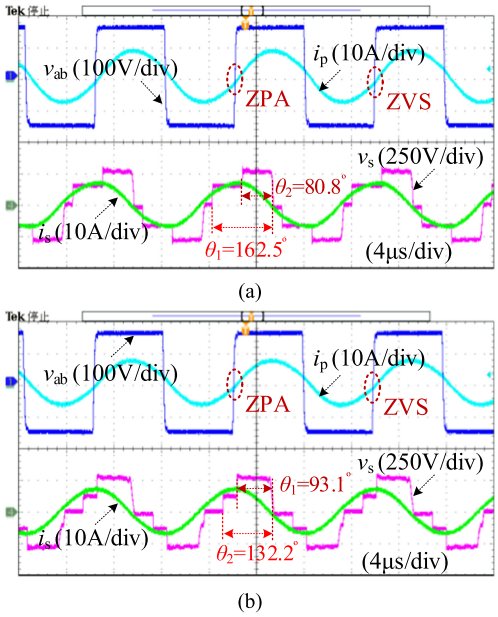

Fig. 18. Experimental waveforms of the multioutput IPT system. (a) SARC1 operates at full load while SARC2 operates at half load. (b) SARC1 operates at half load while SARC2 operates at full load.

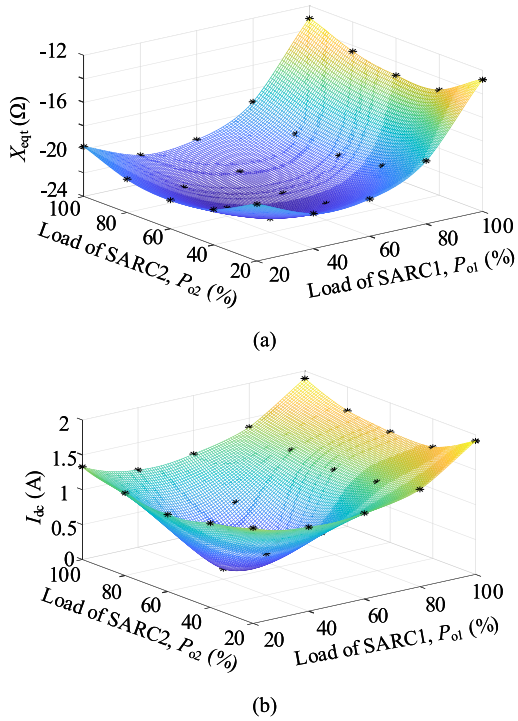

Fig. 19. Total reactance X_{eqt} and the dc bias current I_{dc} versus different P_{oi}. (a) X_{eqt}. (b) I_{dc}.

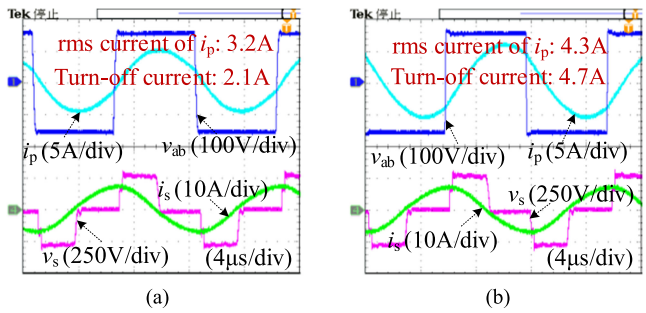

Fig. 20. Experimental waveforms of the multi-output IPT system with/without applying the variable inductor (a) with and (b) without.

A. Steady-State Operation

Fig. 18 shows the steady-state waveforms of the proposed IPT system with $k = 0.3$ when two outputs are under different loads. It should be emphasized that ZVS is obtained by using slightly lagging primary current, but by using better switches with small output capacitance very near ZPA can be ensured as well. As shown in Fig. 18(a), SARC1 operates at full load while SARC2 operates at half load. It can be seen that ZVS for the primary inverter and the SARCi can be ensured. The control angles θ_1 and θ_2 are about 162.5° and 80.8°, respectively. In addition, ZPA of the multioutput IPT system with unity power factor is nearly achieved, which indicates that the Rx side is fully tuned with the variable inductor.

As shown in Fig. 18(b), SARC1 operates at half load while SARC2 operates at full load. It is obvious that ZVS for the primary inverter and the SARCi is also achieved. Meanwhile, the control angles θ_1 and θ_2 are approximately 93.1° and 132.2°, respectively. With the help of the variable inductor, ZPA of the proposed multioutput IPT system with unity power factor can still be maintained.

Fig. 19 shows the experimental results of the total reactance X_{eqt} and the dc bias current I_{dc} when SARCi operates at different load conditions. From Fig. 19, it can be seen that the variation trends of X_{eqt} and I_{dc} versus P_{oi} are nearly the same. As shown in Fig. 19(a), with the decrease of P_{oi}, X_{eqt} decreases and then increases. When X_{eqt} reaches the minimum, a maximum variable inductance is required to maintain unity power factor. Consequently, a minimum I_{dc} is generated by the VCCS, as shown in Fig. 19(b), which agrees with the theoretical analysis.

For comparison, the multioutput IPT system with/without applying the variable inductor was tested when both SARC1 and SARC2 operate at half load, as shown in Fig. 20. It can be seen that the rms current of Tx coil can be reduced from 4.3 A to 3.2 A with applying the variable inductor. Meanwhile, the turn-OFF current of the inverter is reduced from 4.7 A to 2.1 A because of the unity power factor. Consequently, lower conduction loss and switching loss can be achieved, leading to a higher system efficiency. In addition, it can be known from Fig. 20 that the input impedance angle of the proposed IPT system becomes larger without applying the variable inductor. In other words, soft switching of the primary inverter is easier to be obtained under such condition. Hence, the worst case of soft switching realization for main power switches comes when the variable inductor is applied.

B. Dynamic Operation

To validate the dynamic response of the dual outputs without cross regulation, load step for one output is carried out when the other output maintains constant, as shown in Fig. 21. Obviously, the two outputs will not affect each other and the decoupling performance of the proposed IPT system is, thus, verified. From the enlarged view in Fig. 21, it can be found that unity power

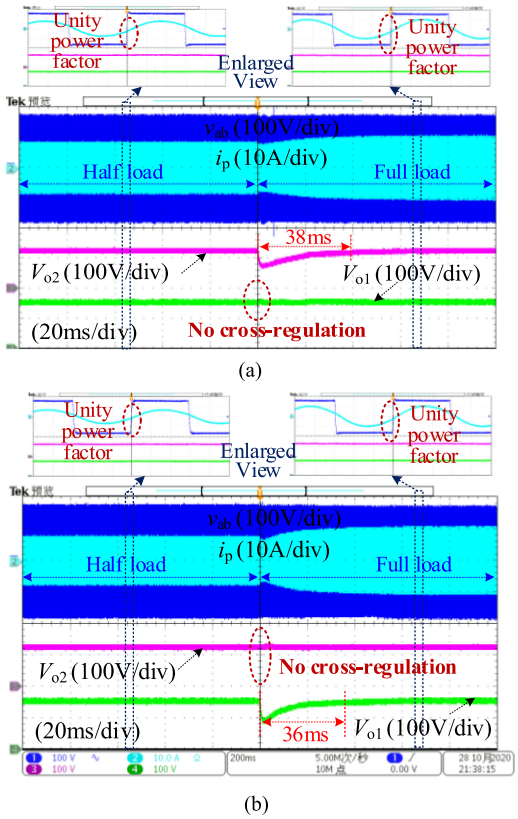

Fig. 21. Experimental waveforms. (a) Load of SARC1 changes from half load to full load. (b) Load of SARC2 changes from half load to full load.

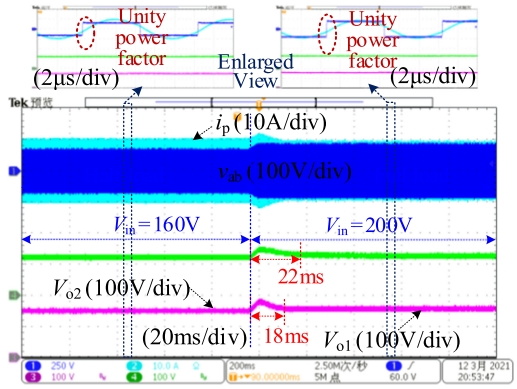

Fig. 22. Experimental waveforms when the input voltage suddenly changes from 160 V to 200 V.

factor of the proposed IPT system is always achieved regardless of the load condition.

Fig. 22 shows the experimental waveforms of the IPT system when the input voltage step changes from 160 V to 200 V. It can be known from Fig. 22 that the output voltages maintain fixed in spite of the input voltage variation. It should be noted that the fluctuations of output voltages are not caused by the cross-regulation issue. From the enlarged view in Fig. 22, it can be found that unity power factor is always guaranteed.

Fig. 23 shows the experimental waveforms of the IPT system when the coupling coefficient k varies from 0.3 to 0.2. With the decrease of k, the Rx coil current i_s increases gradually, which

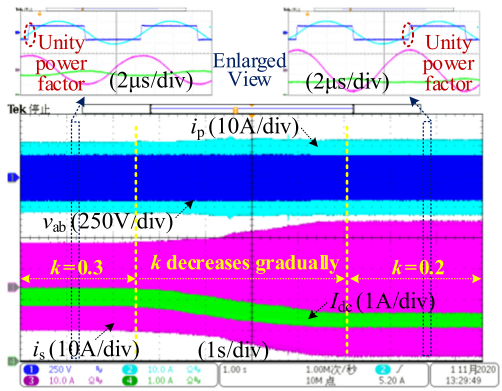

Fig. 23. Experimental waveforms when k varies from 0.3 to 0.2.

indicates the increase of conduction losses. Meanwhile, the bias current I_{dc} decreases slightly to adjust the variable inductance. From the enlarged view in Fig. 23, it can be found that the unity power factor is achieved all the time in spite of the variation of the coupling coefficient. Besides, it can be seen that I_{dc} suffers from large current ripple. That is because the ideal decoupling between the inductor and control windings is not possible due to the nonlinear *B-H* behavior [35], [36]. In other words, the resonant voltage across the inductor winding will induce ac voltage in the control windings.

C. System Efficiency

The measured system efficiency η versus total output power with $V_{in} = 160$ V is shown in Fig. 24(a). It can be found from Fig. 24(a) that the peak efficiency is 96.3% at full load when $k = 0.3$. When $k = 0.2$, the increased Rx coil current results in increased conduction losses and thereby the system efficiency decreases accordingly. Besides, it is clear that the system efficiency with the variable inductor is higher than that without the variable inductor. That is because the variable inductor helps to make the IPT system operate with unity power factor, which can minimize the reactive power losses. The maximum efficiency improvement is approximately 2.1% at 20% load when $k = 0.2$.

Fig. 24(b) shows the measured system efficiency η versus the total output power with different input voltages. With the same output power, the Tx coil current can be decreased when the input voltage increases. However, the Rx coil current increases accordingly, resulting in higher conduction losses. As a result, it can be seen that the efficiency drops slightly with the increase of the input voltage.

It should be noted the winding losses of the variable inductor are ignored in the efficiency curve. However, the core and main winding losses are included because the efficiency is measured by calculating the ratio of the output power to the input power using the power analyzer.

D. Comparison and Discussion

Generally, the multioutput IPT system consists of four parts: the inverter, Tx-side compensation network (including Tx coil), Rx-side compensation network (including Rx coil), and the rectifier. Table IV compares the proposed multioutput scheme

TABLE IV
COMPARISON WITH THE PREVIOUS METHODS

Reference	[16]	[14]	[19]	[13]	[24]	This Work
Number of inverters	n	n	1	1	1	1
Number of Tx-side compensation networks	n	n	n+1	n	1	1
Number of Rx-side compensation networks	n+1	n	n	n	n	1
Number of rectifiers	n	n	n	n	n	n
Unity power factor	No	No	Yes	Yes	Yes	Yes
Individual regulation	No	Yes	No	Yes	No	Yes
Control complexity	Medium	High	Medium	Low	Low	Low
Expansibility	Bad	Medium	Good	Bad	Good	Good
Power capability	Low	Medium	Medium	Low to High	Low to High	Low to High
Galvanic isolation	Yes	No	Yes	Yes	No	No

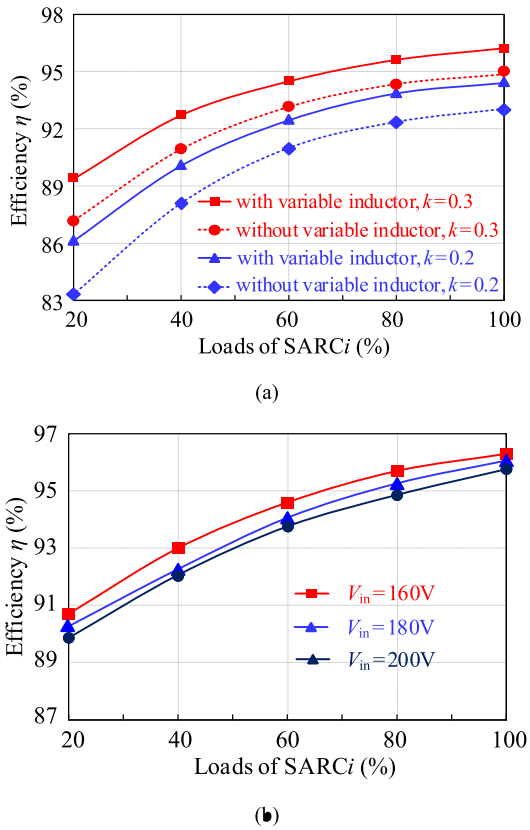

Fig. 24. Measured system efficiency versus the total output power with (a) different coupling coefficients and (b) different input voltages.

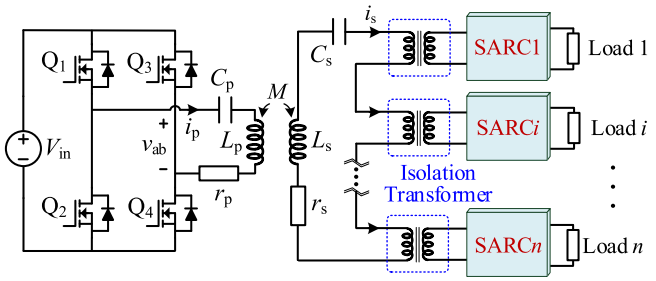

Fig. 25. Multioutput IPT system with complete galvanic isolation by using isolation transformers.

with previous works. These IPT systems are mainly compared in terms of the number of components, unity power factor, individual regulation, control complexity, galvanic isolation, power capability and expansibility, etc.

In [14] and [16], for a total of n outputs, the power stage of the IPT system requires a total of n inverters, which increases the volume and cost significantly. Although one primary inverter is adopted in [13] and [19], multiple Txs are needed to power up for multiple Rxs. Since the mutual couplings between multiple Rxs and the Tx are highly dependent on their relative positions, magnetic coupler design is quite difficult. In [24], multiple compensation networks and corresponding rectifiers are connected in parallel to form multiple independent outputs. However, the outputs cannot be regulated individually. In this article, for a total of n outputs, only the number of rectifiers is n while the number of other parts is one, respectively, leading to low volume and cost. Besides, since there is no cross-regulation issue, the control strategy is simple with good expansibility.

Nevertheless, for the proposed multioutput scheme, there are still some issues remain to be improved. For example, the galvanic isolation among these output channels is not obtained because the SARCs are connected in series. Namely, the loads of the multioutput IPT system should share different grounds. If galvanic isolation is necessary, an isolation transformer can be inserted before each SARC, as shown in Fig. 25.

Although multi-Rx IPT system with separate compensation networks can achieve inherent galvanic isolation [13], [17], the cross-couplings among these Rx coils cannot be avoided, which complicates the circuit modeling and parameter design, even sacrifices the individual regulation performance. It should be

emphasized that additional power losses caused by the isolation transformers may degrade the efficiency. Consequently, from a practical point of view, the designers should consider whether or not the galvanic isolation is required according to their requirements.

Besides, in practical scenarios, the characteristic of constant Tx coil current may be desired so that the IPT system can operate safely even without any secondary side. In this case, the popular current-mode output compensation topologies, such as double-sided *LCC* and *LCC*-parallel, can be used to construct the SARCs-based multioutput IPT systems.

In summary, the proposed multioutput IPT system is simple with good expansibility, which helps promote its development in industry applications. To the best of authors' knowledge, this is the first time that multiple SARCs connected in series are applied to construct the multioutput IPT system. Considering the duality principle, it is possible to utilize multiple voltage-controlled active rectifiers connected in parallel to construct a multioutput IPT system.

V. Conclusion

In this article, a multioutput IPT system based on multiple SARCs is proposed. All SARCs are connected in series at the receiver side and thereby the output voltage of each SARC can be regulated individually. In order to compensate the additional reactance caused by the SARCs, the variable inductor is introduced to maintain the fully resonant condition. An experimental prototype with two outputs 640 W/150 V and 400 W/120 V is built to demonstrate the feasibility and validity of the proposed method. Experimental results show that the two outputs will not affect each other, and unity power factor is always maintained with the help of the variable inductor. Peak efficiency is 96.3% at full load with $k = 0.3$.

References

[1] D. Ahn and S. Hong, "Wireless power transmission with self-regulated output voltage for biomedical implant," *IEEE Trans. Ind. Electron.*, vol. 61, no. 5, pp. 2225–2235, May 2014.

[2] H. Jiang *et al.*, "A low-frequency versatile wireless power transfer technology for biomedical implants," *IEEE Trans. Biomed. Circuits Syst.*, vol. 7, no. 4, pp. 526–535, Aug. 2013.

[3] S. Y. Hui, "Planar wireless charging technology for portable electronic products and qi," *Proc. IEEE*, vol. 101, no. 6, pp. 1290–1301, Jun. 2013.

[4] X. Wang, J. Xu, M. Leng, H. Ma, and S. He, "A hybrid control strategy of LCC-S compensated WPT system for wide output voltage and ZVS range with minimized reactive current," *IEEE Trans. Ind. Electron.*, vol. 68, no. 9, pp. 7908–7920, Sep. 2021.

[5] G. R. Kalra, B. S. Riar, and D. J. Thrimawithana, "An integrated boost active bridge based secondary inductive power transfer converter," *IEEE Trans. Power Electron.*, vol. 35, no. 12, pp. 12716–12727, Dec. 2020.

[6] Z. Huang, S. Wong,, and C. K. Tse, "Design of a single-stage inductive-power-transfer converter for efficient EV battery charging," *IEEE Trans. Veh. Technol.*, vol. 66, no. 7, pp. 5808–5821, Jul. 2017.

[7] J. Deng, W. Li, T. D. Nguyen, S. Li, and C. C. Mi, "Compact and efficient bipolar coupler for wireless power chargers: Design and analysis," *IEEE Trans. Power Electron.*, vol. 30, no. 11, pp. 6130–6140, Nov. 2015.

[8] K. Yoon, S. Lee, I. Cho, H. Lee, and G. Cho, "Dual receiver coils wireless power transfer system with interleaving switching," *IEEE Trans. Power Electron.*, vol. 33, no. 12, pp. 10016–10020, Dec. 2018.

[9] C. Jiang, K. T. Chau, T. W. Ching, C. Liu, and W. Han, "Time-division multiplexing wireless power transfer for separately excited DC motor drives," *IEEE Trans. Magn.*, vol. 53, no. 11, pp. 1–5, Nov. 2017.

[10] N. U. Hassan, S. Hong, and B. Lee, "A robust multi-output self-regulated rectifier for wirelessly-powered biomedical applications," *IEEE Trans. Ind. Electron.*, vol. 68, no. 6, pp. 5466–5472, Jun. 2021.

[11] J. Hu *et al.*, "Hybrid energy storage system of an electric scooter based on wireless power transfer," *IEEE Trans. Ind. Informat.*, vol. 14, no. 9, pp. 4169–4178, Sep. 2018.

[12] M. McDonough, "Integration of inductively coupled power transfer and hybrid energy storage system: A multiport power electronics interface for battery-powered electric vehicles," *IEEE Trans. Power Electron.*, vol. 30, no. 11, pp. 6423–6433, Nov. 2017.

[13] V. Vu, V. Phan, M. Dahidah, and V. Pickert, "Multiple output inductive charger for electric vehicles," *IEEE Trans. Power Electron.*, vol. 34, no. 8, pp. 7350–7368, Aug. 2019.

[14] A. T. L. Lee, W. Jin, S. Tan, and S. Y. Hui, "Buck-boost single-inductor multiple-output high-frequency inverters for medium-power wireless power transfer," *IEEE Trans. Power Electron.*, vol. 34, no. 4, pp. 3457–3473, Apr. 2019.

[15] W. Jin, A. T. L. Lee, S. Tan, and S. Y. Hui, "A gallium nitride (GaN)-based single-inductor multiple-output (SIMO) inverter with multi-frequency AC outputs," *IEEE Trans. Power Electron.*, vol. 34, no. 11, pp. 10856–10873, Nov. 2019.

[16] M. Q. Nguyen, Y. Chou, D. Plesa, S. Rao, and J.- C. Chiao, "Multiple-inputs and multiple-outputs wireless power combining and delivering systems," *IEEE Trans. Power Electron.*, vol. 30, no. 11, pp. 6254–6263, Nov. 2015.

[17] L. Sun, H. Tang, and S. Zhong, "Load-independent output voltage analysis of multiple-receiver wireless power transfer system," *IEEE Antennas Wireless Propag. Lett.*, vol. 15, pp. 1238–1241, 2015.

[18] D. Ahn, S. Kim, S. Kim, J. Moon, and I. Cho, "Wireless power transfer receiver with adjustable coil output voltage for multiple receivers application," *IEEE Trans. Ind. Electron.*, vol. 66, no. 5, pp. 4003–4012, May 2019.

[19] C. Cheng, W. Li, Z. Zhou, Z. Deng, and C. Mi, "A load-independent wireless power transfer system with multiple constant voltage outputs," *IEEE Trans. Power Electron.*, vol. 35, no. 4, pp. 3328–3331, Apr. 2020.

[20] Z. Pantic, K. Lee, and S. M. Lukic, "Receivers for multifrequency wireless power transfer: Design for minimum interference," *IEEE J. Emerg. Sel. Topics Power Electron.*, vol. 3, no. 1, pp. 234–241, Mar. 2015.

[21] C. Cheng, Z. Zhou, W. Li, C. Zhu, Z. Deng, and C. Mi, "A multiload wireless power transfer system with series-parallel-series compensation," *IEEE Trans. Power Electron.*, vol. 34, no. 8, pp. 7126–7130, Aug. 2019.

[22] M. Budhia, J. T. Boys, G. A. Covic, and C. Huang, "Development of a single-sided flux magnetic coupler for electric vehicle IPT charging systems," *IEEE Trans. Ind. Electron.*, vol. 60, no. 1, pp. 318–328, Jan. 2013.

[23] Y. Li, R. Mai, L. Lu, T. Lin, Y. Liu, and Z. He, "Analysis and transmitter currents decomposition based control for multiple overlapped transmitters based WPT systems considering cross couplings," *IEEE Trans. Power Electron.*, vol. 33, no. 2, pp. 1829–1842, Feb. 2018.

[24] Y. Li *et al.*, "Analysis, design, and experimental verification of a mixed high-order compensations-based WPT system with constant current outputs for driving multistring LEDs," *IEEE Trans. Ind. Electron.*, vol. 67, no. 1, pp. 203–213, Jan. 2020.

[25] Y. Li, J. Hu, X. Li, and K. E. Cheng, "A flexible load-independent multi-output wireless power transfer system based on cascaded double T-Resonant circuits: Analysis, design and experimental verification," *IEEE Trans. Circuits Syst. I, Reg. Papers*, vol. 66, no. 7, pp. 2803–2812, Jul. 2019.

[26] Z. Huang, C. Lam, P. Mak, R. P. D. S. Martins, S. Wong, and C. K. Tse, "A single-stage inductive-power-transfer converter for constant-power and maximum-efficiency battery charging," *IEEE Trans. Power Electron.*, vol. 35, no. 9, pp. 8973–8984, Sep. 2020.

[27] K. Colak, E. Asa, M. Bojarski, D. Czarkowski, and O. C. Onar, "A novel phase-shift control of semibridgeless active rectifier for wireless power transfer," *IEEE Trans. Power Electron.*, vol. 30, no. 11, pp. 6288–6297, Nov. 2015.

[28] I. Iam *et al.*, "Constant-frequency and non-communication-based inductive power transfer converter for battery charging," *IEEE J. Emerg. Sel. Topics Power Electron.*, doi: 10.1109/JESTPE.2020.3004259.

[29] T. Diekhans and R. W. De Doncker, "A dual-side controlled inductive power transfer system optimized for large coupling factor variations and partial load," *IEEE Trans. Power Electron.*, vol. 30, no. 11, pp. 6320–6328, Nov. 2015.

[30] R. Mai, Y. Liu, Y. Li, P. Yue, G. Cao, and Z. He, "An active- rectifier-based maximum efficiency tracking method using an additional measurement coil for wireless power transfer," *IEEE Trans. Power Electron.*, vol. 33, no. 1, pp. 716–728, Jan. 2018.

[31] X. Wang, J. Xu, H. Ma, and S. He, "Inductive power transfer systems with digital switch-controlled capacitor for maximum efficiency point tracking," *IEEE Trans. Ind. Electron.*, vol. 68, no. 10, pp. 9467–9480, Oct. 2021.

[32] J. Zhang, J. Zhao, Y. Zhang, and F. Deng, "A wireless power transfer system with dual switch-controlled capacitors for efficiency optimization," *IEEE Trans. Power Electron.*, vol. 35, no. 6, pp. 6091–6101, Jun. 2020.
[33] A. Kamineni, G. A. Covic, and J. T. Boys, "Self-tuning power supply for inductive charging," *IEEE Trans. Power Electron.*, vol. 32, no. 5, pp. 3467–3479, May 2017.
[34] Y. Lim, H. Tang, S. Lim, and J. Park, "An adaptive impedance-matching network based on a novel capacitor matrix for wireless power transfer," *IEEE Trans. Power Electron.*, vol. 29, no. 8, pp. 4403–4413, Aug. 2014.
[35] Z. Zhang, F. Zhu, D. Xu, P. T. Krein, and H. Ma, "An integrated inductive power transfer system design with a variable inductor for misalignment tolerance and battery charging applications," *IEEE Trans. Power Electron.*, vol. 35, no. 11, pp. 11544–11556, Nov. 2020.
[36] M. S. Perdigão, "Research and development on new control techniques for electronic ballasts based on magnetic regulators," Ph.D. dissertation, Dept. Elect. Comput. Eng., Univ. Coimbra, Coimbra, Portugal, Jun. 2012.
[37] Y. Hu, L. Huber, and M. M. Jovanovic, "Single-stage universal-input AC/DC LED driver with current-controlled variable PFC boost inductor," *IEEE Trans. Power Electron.*, vol. 27, no. 3, pp. 1579–1588, Mar. 2012.
[38] M. S. Perdigo, J. M. Alonso, M. A. Dalla Costa, and E. S. Saraiva, "Using magnetic regulators for the optimization of universal ballasts," *IEEE Trans. Power Electron.*, vol. 23, no. 6, pp. 3126–3134, Nov. 2008.
[39] D. Medini and S. Ben-Yaakov, "A current-controlled variable-inductor for high frequency resonant power circuits," in *Proc. IEEE Appl. Power Electron. Conf. Expo.*, Orlando, FL, USA, 1994, pp. 219–225.
[40] S. Huang, T. Lee, W. Li, and R. Chen, "Modular on-road AGV wireless charging systems via interoperable power adjustment," *IEEE Trans. Ind. Electron.*, vol. 66, no. 8, pp. 5918–5928, Aug. 2019.
[41] M. Lu and K. D. T. Ngo, "Systematic design of coils in series–series inductive power transfer for power transferability and efficiency," *IEEE Trans. Power Electron.*, vol. 33, no. 4, pp. 3333–3345, Apr. 2018.
[42] Z. Luo, X. Wei, M. G. S. Pearce, and G. A. Covic, "Multi-objective optimization of inductive power transfer double-D pads for electric vehicles," *IEEE Trans. Power Electron.*, vol. 36, no. 5, pp. 5135–5146, May 2021.
[43] X. Tang, J. Zeng, K. P. Pun, S. Mai, C. Zhang, and Z. Wang, "Low-cost maximum efficiency tracking method for wireless power transfer systems," *IEEE Trans. Power Electron.*, vol. 33, no. 6, pp. 5317–5329, Jun. 2018.
[44] R. Mai, P. Yue, Y. Liu, Y. Zhang, and Z. He, "A dynamic tuning method utilizing inductor paralleled with load for inductive power transfer," *IEEE Trans. Power Electron.*, vol. 33, no. 12, pp. 10924–10934, Dec. 2018.
[45] S. Lee B. Choi and C. T. Rim, "Dynamics characterization of the inductive power transfer system for online electric vehicles by laplace phasor transform," *IEEE Trans. Power Electron.*, vol. 28, no. 12, pp. 5902–5909, Dec. 2013.
[46] A. C. Bagchi, H. Wang, T. Saha, and R. Zane, "Small-signal phasor modeling of an underwater IPT system in constant current distribution," in *Proc. IEEE Appl. Power Electron. Conf. Expo.*, 2019, pp. 876–883.

Xiaoqiang Wang received the B.S. degree in electrical engineering in 2016 from Southwest Jiaotong University, Chengdu, China, where he is currently working toward the Ph.D. degree with the School of Electrical Engineering.

His research interests include wireless power transfer and resonant converter.

Jianping Xu (Member, IEEE) received the B.S. and Ph.D. degrees in electronic engineering from the University of Electronics Science and Technology of China, Chengdu, China, in 1984 and 1989, respectively.

Since 1989, he has been with the School of Electrical Engineering, Southwest Jiaotong University, Chengdu, China, where he has been a Professor since 1995. From November 1991 to February 1993, he was with the Department of Electrical Engineering, University of Federal Defense Munich, Germany, as a Visiting Research Fellow. From February 1993 to July 1994, he was with the Department of Electrical Engineering and Computer Science, University of Illinois at Chicago, Chicago, IL, USA, as a Visiting Scholar. His research interests include the modeling, analysis, and control of power electronic systems.

Song Lu received the B.S. degree in electrical engineering in 2017 from Southwest Jiaotong University, Chengdu, China, where he is currently working toward the Ph.D. degree.

His research interests include power factor correction and resonant converters.

Sheng Ren was born in Sichuan, China, in 1997, He received the B.S. degree in electrical engineering and automation from Southwest Petroleum University, Chengdu, China, in 2019. He is currently working toward the Ph.D. degree in electrical engineering with the Southwest Jiaotong University, Chengdu, China.

His main research interests include wireless power transfer.

Minrui Leng (Student Member, IEEE) received the B.S. degree in electrical engineering and automation in 2014 from Southwest Jiaotong University, Chengdu, China, where she is currently working toward the Ph.D. degree with the School of Electrical Engineering.

She has been a Visiting Ph.D. Student with the Department of Energy Technology, Aalborg University, Aalborg, Denmark, since 2019. Her research interests include small signal modelling and dynamical modeling of power converter, control techniques of power converter, stability of distributed power systems, and model predictive control of dc microgids.

Hongbo Ma (Member, IEEE) received the B.S. degree from Lanzhou Jiaotong University, Lanzhou, China, in 2004, and Ph.D. degree from the Southwest Jiaotong University, Chengdu, China, in 2012, both in electrical engineering.

From September 2009 to October 2011, he was a Research Assistant at the Future Energy Electronics Center, Virginia Polytechnic Institute and State University, Blacksburg, Virginia. From December 2012 to July 2013, he was a Postdoctoral Researcher with the National Taiwan University of Science and Technology, Taipei, Taiwan. He is currently an Associate Professor with the School of Electrical Engineering, Southwest Jiaotong University, China. Meanwhile, he is also a Research Fellow with the Power Electronics Center, NTUST, Taipei, Taiwan. He has authored or coauthored more than 80 technical papers. His research interests include high-efficiency/high power density power converters, wireless power transfer system, MHz power supply module with wide bandgap devices, and power supply for aeronautics and astronautics applications.